Tech : Journal of Engineering Science
Vol. 2, No. 2, 2026.
e-ISSN: 3109-7790 (online)
https://jurnal.sinesia.id/index.php/tech/index

Investigating the Viscosity-Pressure Drop Trade-Off and Hydrodynamic Penalties in Nanofluid-Enhanced Cooling Loops

Obinani Victor Chimdike[1], Olusegun David Samuel[2], Chinedum Ogonna Mgbemena[3]
E-mail Korespondensi : cv.obinani@unizik.edu.ng
[1]Nnamdi Azikiwe University, Awka, Anambra State, Nigeria.
[2,3]Federal University of Petroleum Resources, Effurun, Delta State, Nigeria.

Info Article
|Submitted: 24 July 2026 **|Revised**: 9 August 2026 **|Accepted**: 11 August 2026
|Published: 11 August 2026
How to Cite : Obinani Victor Chimdike, etc., "Investigating the Viscosity-Pressure Drop Trade-Off and Hydrodynamic Penalties in Nanofluid-Enhanced Cooling Loops", *Tech: Journal of Engineering Scince*, Vol. 2, No. 2, 2026, P. 217-235.

ABSTRACT

This research explores the non-linear thermofluidic trade-offs in a thermal management loop for solid-state thermoelectric cooling (TEC) applications in the presence of nanoparticles. Although nanofluids convey a significant advantage in the convective heat transfer, the presence of a significant increase in dynamic viscosity of the nanofluid considerably limits its application, leading to an increase in pumping power. A stable Nanofluid of alumina-water ($Al_2O_3 - H_2O$) with alpha phase alumina was synthesized using the two-step method with a fixed ratio (1:1) using the stabilizer of Sodium Dodecylbenzene Sulfonate (SDBS). The Face-Centered Central Composite Design (CCD) was used to run 27 different parametric runs with a multi-variable experimental matrix. Three diameters of the nanoparticles (10 nm, 30 nm, and 50 nm), three volume fractions (2.0%, 4.0% and 5.0% vol.), and three volumetric flow rates (0.5 L/min, 1.2 L/min, and 2.4 L/min) were selected to encompass the laminar, transitional, and turbulent flow regimes. The performance of the system was determined by measuring the hot and cold junction temperature (T_h, T_c), system COP ($COP_{cooling}$), microchannel friction factors (fnf), and drop in core line pressure (ΔP). To minimize error, theoretical reduction models were used, such as Corcione's viscosity correlation and Leong's stationary nanolayer thermal reduction model. System level multi-objective optimization at a 2.36L/min flow rate was able to define a clear "sweet spot" envelope. The best combination is obtained when using 29.60 nm nanoparticles with a volume fraction of 4.18% vol., which leads to a minimum dynamic viscosity of $0.000891 Pa \cdot s$, a well-controlled pressure drop of 10.52 Pa and maximized Performance Evaluation Criterion (PEC = 1.065). This empirical boundary shows that targeted particle nesting can be an effective way to avoid the large degradation of hydrodynamic performance at the hot-side thermal resistance limit (hydrodynamic degradation >5.0% vol.) and the clogging of the cooling loops by particles (clogging >5.0% vol.), and gives a clear mathematical recipe for reducing the hot-side thermal resistance without the hydrodynamic and clogging degradation.

Keywords: *Nanofluids, Thermoelectric Cooling (TEC), Pressure Drop, Performance Evaluation Criterion (PEC), Multi-Objective Optimization, and Viscosity Trade-Off*

Introduction

With the fast development of high heat flux systems, the conventional thermal management infrastructures are reaching their physical limits (Lim & Yu, 2025). Localized heat dissipation needs often surpass 100 W/cm^2 in modern applications in microelectronics, next generation data centers and Electric Vehicles (EVs) battery packs (Lau & Fan, 2025; Kalantarpour & Vafai, 2024; Egin Martin et al., 2025). The conventional cooling architectures are very dependent on the single-phase convective heat transfer, with the use of conventional base fluids like water, ethylene glycol and mineral oils (Murshed & de Castro, 2017). But these traditional

This work is licensed under CC BY-SA 4.0

liquids are literally limited by their poor thermal conductivity properties, which leads to a significant thermal resistance barrier, with the potential for catastrophic degradation of components, hot spots and a dramatic loss of efficiency. Therefore, overcoming the thermal transport limit of traditional single-phase liquids is a key goal of the advanced thermal design engineer (Moita et al., 2021).

To overcome these structural barriers, nanofluid cooling loops have become a leading active heat transport solution (Porgar et al., 2024). The overall properties of the nanofluids are found to be anomalous with respect to the effective thermal conductivity and convective heat transfer coefficient (Damodaran, 2012) and are obtained by adding the engineered nanometer size particles (<100 nm) to a base liquid in the form of a colloidal suspension. When highly conductive metal-oxide nanostructures (like alpha-phase alumina (Al_2O_3), metals, carbides, or carbon nanostructures (CNTs, Graphene, etc.) are added, sub-micron thermal enhancement mechanisms (Mirsafi et al., 2026) are activated. These mechanisms involve localized mixing in Brownian motion, high conductivity interatomic fluid layering at the liquid-solid boundary, and massive enhancement in the surface area available for heat exchange (Cui et al., 2015; Mishra et al., 2020). For instance, nanofluids have been observed to consistently achieve significant decreases in hot-side thermal resistance, and even significant enhancements to the cooling loop Coefficient of Performance (COP) in compact applications such as microchannel heat sinks (Cui et al., 2015; Ma et al., 2023; Myat et al., 2025).

These particle-scale mechanisms, however, do not survive intact as the loop is scaled up to a working flow. Brownian micro-convection and interfacial layering are diffusive, low-energy processes, so their contribution to total transport is measurable only where bulk advection is weak; that is, in the laminar and lower transitional regimes and is progressively masked once turbulent eddy mixing begins to dominate the energy balance. At the same time, the very features responsible for the thermal gain govern momentum transport as well: a particle cluster that bridges heat across the fluid also resists shear across it. The microscopic origin of the enhancement and the macroscopic hydrodynamic cost are thus two readings of the same physics, and neither can be evaluated without specifying the flow regime in which the loop operates.

This coupling of scales is precisely what the current literature leaves unresolved. Most of the published studies are devoted exclusively to maximizing thermal conductivity enhancements (Ayyappan et al., 2026) and minimize or even ignore the severe concurrent hydrodynamic penalties. Solid nanoparticles get trapped in the suspension and the dynamic viscosity of the fluid is greatly increased because of internal shear resistance and nanoparticle aggregation (Myat et al., 2025). The Darcy-Weisbach model indicates that the viscosity increase in these small-scale

geometries results in an exponential increase in the line pressure drop (ΔP) across the system (Herbst et al., 2025), thereby exponentially increasing the parasitic pumping power requirement of the system (Yildirim et al., 2026). This is a significant engineering trade-off as the relative pumping power penalty grows at a faster rate than the convective heat transfer coefficient and results in a decrease in thermodynamic efficiency of the system, thereby making the nanofluid modification ineffective (Chavda et al., 2015).

Resolving that trade-off requires observing both scales simultaneously rather than in isolation. This study therefore performs a multi-variable experimental investigation of an electrostatically stabilized microchannel loop, mapping performance continuously across the laminar, transitional, and turbulent regimes using a Face-Centered Central Composite Design (CCD). Doing so isolates the exact velocity thresholds at which shear disrupts particle clusters and the fluid transitions into Newtonian stabilization — the point at which the microscopic mechanisms described above cease to control macroscopic behavior. The paper concludes by presenting a concrete multi-objective operational envelope and provides a mathematical proof for the exact boundaries in terms of nanoparticle size and concentration that define the optimization of thermal dissipation without incurring any destructive penalty related to hydrodynamics.

Research Methods

Nanofluid Preparation and Stabilization

Base Fluid: Deionized (DI) water ($\rho = 997 kg/m^3$ $\mu = 0.00089\ Pa.s$ at 25°C).

Nanoparticles: Alpha-phase Aluminum Oxide ($\alpha - Al_2O_3$, density $\rho_p = 3900\ kg/m^3$ varied across three nominal diameters (d_p= 10nm, 30nm, 50 nm). The alpha-phase alumina-water (Al_2O_3-H_2O) nanofluids used in the present work were prepared by the conventional two-step method. This method was chosen to separate the synthesis of nanoparticles from the dispersion in liquid, enabling the precise management of the multi variable experimental matrix in terms of volume. The first dispersed phases were commercial grade alpha-($Al_2O_3 - H_2O$) dry nano powders with a nominal spherical particle diameter of 10 nm, 30 nm and 50 nm. All formulation runs were tested with ultrapure deionized (DI) water as a base fluid. A chemical stabilization strategy was used to reduce the strong surface-energy forces and counteract the spontaneous macro-agglomeration that would occur in the microchannel cooling loop. An anionic surfactant, Sodium Dodecylbenzene Sulfonate (SDBS) was chosen as the dispersing agent. The mass ratio of the nanoparticles to SDBS, was kept at 1:1 in all the test conditions for optimizing the stability of the suspension and minimizing the thermal resistance induced by the surfactant. The sequential preparation protocol was performed:

Mass Measurement

The mass of dry Al_2O_3 nanoparticles required to achieve the target volume fractions (2.0%, 4.0%, and 5.0% vol.) was precisely measured using an analytical microbalance with an accuracy of ±0.1 mg.



Figure 1. SDBS surfactant powder measured on an analytical balance

Surfactant Dissolution

An equal mass of SDBS surfactant (1:1 weight ratio relative to the measured nano powder) was added to a predetermined volume of DI water. The mixture was mechanically stirred for 15 minutes to guarantee complete dissolution and uniform surfactant monomer distribution in the base fluid.



Figure 2: Preparation steps for the bulk solution: (a) raw SDBS powder, (b) powder sampling, and (c) final mixture in the bulk container.

Dry Powder Incorporation

The dry Al_2O_3 nanoparticles (10 nm, 30 nm, or 50 nm) were gradually introduced into the aqueous SDBS solution under continuous, low-speed magnetic stirring to form an initial, crude macro-suspension.

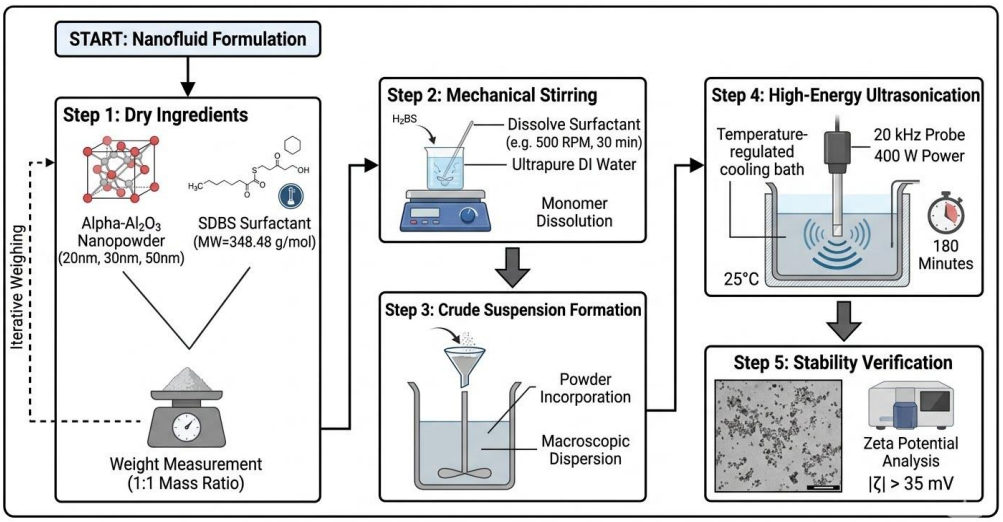


Figure 3. Process flow diagram for Al_2O_3/SDBS nanofluid preparation and stability testing

Ultrasonic Disaggregation:

To break down tightly bound agglomerate clusters via acoustic cavitation, the crude suspension was subjected to high-energy probe ultrasonication (20 kHz, 400 W output power) for a continuous duration of 180 minutes. To prevent excessive fluid heating and surfactant thermal degradation during this high-energy phase, the sample vessel was submerged in a temperature-controlled cold-water bath maintained at 25°C.

Nanofluid Loop Architecture

Microchannel Loop Experimental Setup

To evaluate the hydrodynamic penalties and core line pressure drops of the formulated Al_2O_3-H_2O nanofluids, a closed-loop fluid distribution system was constructed. The primary design objective of the test rig was to isolate the fluid friction losses across the microchannel geometry under tightly monitored thermal and flow boundary conditions. The flow loop comprised five major operational assemblies arranged in a closed circuit: a fluid reservoir, a variable-speed pump, a microchannel test section integrated with a thermoelectric cooling (TEC) assembly, a secondary liquid-to-air heat exchanger, and inline instrumentation.

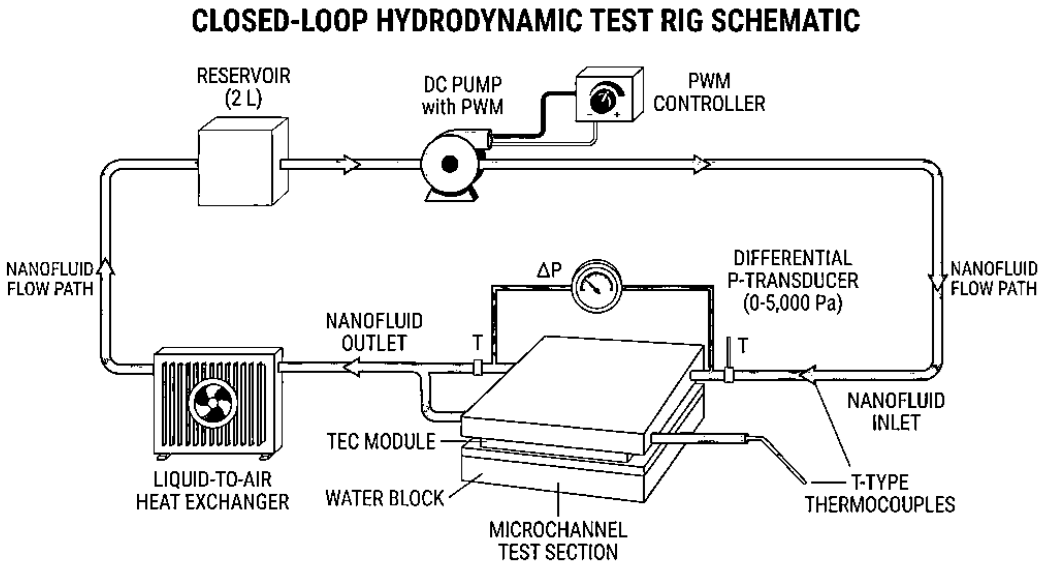


Figure 4. Schematic Diagram of the Closed-Loop Hydrodynamic Experimental Test Rig.

The fluid was circulated via a 12v DC pump capable of supplying smooth, pulse-free volumetric flow rates across the target range of 0.5 to 2.4 L/min. To monitor and maintain the strict flow velocities required by the experimental matrix, a PWM controller is attached to the pump with an operating accuracy of ±1.0% was positioned immediately downstream of the pump discharge. The fluid then entered the primary microchannel test section; The microchannel assembly was clamped securely between a solid-state thermoelectric cooling (TEC) module and a high-accuracy water block to simulate electronic hot-junction dissipation profiles. To capture the absolute hydrodynamic penalties without interference from external piping geometry, instrument ports were connected directly into the inlet and outlet manifolds of the microchannel block.

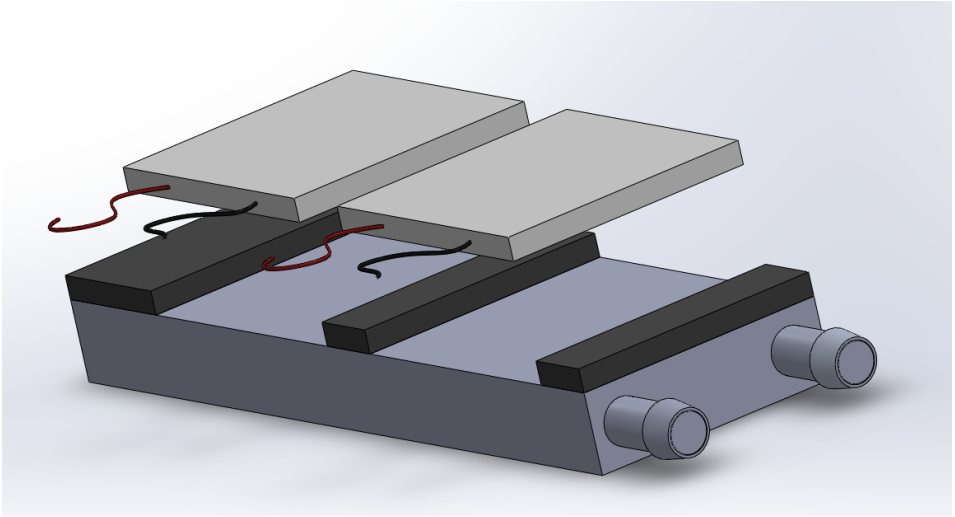


Figure 5 Exploded CAD Rendering of the Microchannel Liquid Cooling Block Stack Integrated with Solid-State Thermoelectric Cooling (TEC) Modules.

After exiting the microchannel test section, the heated nanofluid was routed through a secondary liquid-to-air finned heat exchanger to reject accumulated thermal energy and return the fluid to a stable ambient baseline temperature of $27°C$. The stabilized fluid was then collected in a sealed 2L reservoir before being re-drawn by the pump, ensuring a constant, bubble-free supply of fluid throughout the 27 distinct experimental runs.

Loop Maintenance and Anti-Sedimentation Protocol

To preserve structural repeatability and eliminate data drift from particle fouling, a rigorous loop maintenance lifecycle is executed between every single test configuration:

1. System Drain: The active nanofluid sample is completely evacuated from the closed loop.
2. Primary DI Flush: The loop is filled with pure deionized water and driven at maximum pump velocity ($Re \approx 4000$) for 15 minutes to dislodge particles caught in low-velocity recirculation zones.
3. Chemical Scour: A mild 0.1M acidic flush is introduced if any structural scaling or surface staining is visually detected on the microchannels.
4. Final Rinse & Verification: The system is flushed with fresh DI water until the baseline differential pressure matches the original calibration benchmark ($\Delta P_{baseline} \pm 1.2\%$). The loop is completely dried using compressed nitrogen gas before introducing a new nanofluid concentration.

Mathematical Modeling of Hydrodynamic Parameters

Brinkman Model for Nanofluid Viscosity

To isolate the geometric and thermal mechanisms driving fluid shear stress, the experimental dynamic viscosity (μ_{nf}) is calculated using an extension of Einstein's equation that factors in the hydrodynamic interactions between neighboring particles as the mixture thickens Accounts for moderate concentration packing effects by extending Einstein's continuum mechanics as indicated in Eq. (1)

$$\mu_{nf} = \frac{\mu_{bf}}{(1-\phi)^{2.5}} \qquad (1)$$

Corcione Empirical Correlation for Nanofluid Viscosity

Classical models fail for particles under 50nm because they ignore the high surface-area energy and Brownian motion effects. For alumina-water nanofluids, Corcione's widely verified empirical model mathematically accounts for fluid

temperature (T), nanoparticle diameter (d_p), and concentration (ϕ) as shown in Eq. (2).

The negative exponent on particle size ensures that as d_{np} decreases, the denominator shrinks, causing the calculated viscosity μ_{nf} to correctly rise.

Eq. (3a) might be adopted to determine the dynamic viscosity of the nanofluid while determining the empirical relationship between nanofluid viscosity, volume fraction and particle diameter using Eq. (3b).

$$\mu_{nf} = \frac{\mu_{bf}}{1 - 34.87.\left(\frac{d_{np}}{d_{bf}}\right)^{-0.3}.\phi^{1.03}} \quad (2)$$

μ_{nf}= Dynamic viscosity of the nanofluid ($Pa.s$)

μ_{bf} = Dynamic viscosity of the pure base fluid = $0.89mPa$

ϕ = Volume fraction of nanoparticles (expressed as a decimal, e.g., 1% = 0.01)

d_{np} = Nanoparticle diameter (m)

d_{bf} = Equivalent diameter of a base fluid molecule, calculated via fluid density and molecular weight. For pure water, $d_{bf} = 0.29nm = 2.9 \times 10^{-10}m$

$$\mu_{nf} = \frac{0.89\times10^{-3}}{1-34.87.\left(\frac{d_{np}}{2.9\times10^{-10}}\right)^{-0.3}.\phi^{1.03}} \quad (3a)$$

$$\mu_{nf} = \frac{0.89 \times 10^{-3}}{1 - 0.048.{d_{np}}^{-0.3}.\phi^{1.03}} \quad (3b)$$

Flow Modulation and Reynolds Number Classification

The experimental fluid loop actively modulates the mass flow rate using a PWM-controlled magnetic drive pump to push the fluid through three distinct hydrodynamic regimes. The characterization is governed by the hydraulic Reynolds number (Re) as shown in Eq. (4).

$$Re = \frac{\rho_{nf} v D_h}{\mu_{nf}} \quad (4)$$

Where (v) is the mean fluid velocity and (D_h) is the channel hydraulic diameter.

The flow regimes are classified into three test windows:

Laminar Zone ($500 \leq Re < 2000$): Dominated by viscous forces; velocity profile is parabolic.

Transitional Zone ($2000 \leq Re \leq 3000$): Characterized by intermittent turbulent bursts and unstable flow signatures.

Turbulent Boundary ($3000 < Re \leq 4000$): Dominated by inertial core mixing and sub-layer viscous shears.

Friction Evaluation and Intermittency Scaling

To capture the exact flow resistance across unstable regions, the Darcy friction factor (f) is calculated from experimental data. In the fully laminar regime, the theoretical baseline is tracked via the modified Hagen-Poiseuille friction model as indicated in Eq. 5.

$$f_{lam} = \frac{64}{Re} \qquad (5)$$

In the transitional zone, standard linear interpolations fail due to sudden turbulent slug formations. This methodology integrates an intermittency factor (γ_{int}) scaling mechanism to determine the transitional friction coefficient. Eq. 6 gives an expression for the friction model for a transitional phase.

$$f_{trans} = (1 - \gamma_{int}) f_{lam} + \gamma_{int} f_{turb} \qquad (6)$$

The intermittency factor swings dynamically ($0 \leq \gamma_{int} \leq 1$) based on statistical velocity fluctuation peaks captured by the flow sensors. The fully turbulent baseline (f_{turb}) is cross-referenced using the Blasius correlation ($f_{turb} = 0.3164.Re^{-0.25}$).

The Viscosity–Pressure Drop Trade-off

While nanoparticles improve thermal performance, they simultaneously introduce a mechanical "cost." This study uses the Darcy-Weisbach Equation to theorize the relationship between fluid properties and energy consumption as shown in Eq. (7):

$$\Delta P = f.\frac{L}{D}\frac{\rho v^2}{2} \qquad (7)$$

The theory suggests that as the concentration (ϕ) of Al_2O_3 increases, the dynamic viscosity of the fluid rises. This leads to a higher friction factor (f), which necessitates a greater pressure drop (ΔP) to maintain the flow. Consequently, the pumping power (P_{pump}) increases, which represents a parasitic load that can potentially negate the COP gains of the TEC module.

Performance Evaluation Criterion (PEC)

To mathematically confirm the thermodynamic viability of replacing the base liquid with the Al_2O_3 nanofluid, the Performance Evaluation Criterion (PEC) is used to track the thermal-to-hydraulic balance. PEC is expressed in Eq. 8 as a ratio of

Nusselt number enhancement ratio to the cube root of friction factor enhancement ratio under constant pumping power.

$$PEC = \frac{Nu_{nf} / Nu_{bf}}{\left(f_{nf} / f_{bf}\right)^{\frac{1}{3}}} \quad (7)$$

Where Nu_{nf} and Nu_{bf} represent the Nusselt numbers for the nanofluid and base fluid, respectively. A calculated **PEC > 1.0** indicates that the enhancement in convective heat transfer exceeds the relative pumping power penalty, verifying that the system is operating within a sustainable thermal envelope.

Empirical Verification (2.0% Vol. Formulation Baseline)

To demonstrate the physical alignment of this framework for a 2 Liter (2,000 cm³) cooling loop system, the quantitative parameter baseline for the 2.0% volume concentration run is derived as follows:

Target Volume Fraction (ϕ) = 2.0%

Total Fluid Volume (V_{total}) = 2,000 cm³

$\alpha - phase\ Al_2O_3$ Density (ρ_{np}) = 3.95 g/cm³

m_{np} = Measured mass of the dry Al_2O_3 nanoparticles (g).

$$m_{np} = (2.0 / 100) * 2{,}000\ cm^3 * 3.95\ g/cm^3 = 158.0\ grams$$

The physical volume occupied by these solid particles is:

$$V_{np} = 158.0\ g / 3.95\ g/cm^3 = 40.0\ cm^3$$

Consequently, the precise volume of deionized base water required to achieve a true 2L final mixture volume is isolated by subtracting the particle volume from the total target threshold:

$$V_{bf} = V_{total} - V_{np} = 2{,}000\ cm^3 - 40.0\ cm^3 = 1{,}960.0\ cm^3\ (or\ 1{,}960.0\ mL)$$

This mathematical reduction guarantees that the physical fluid density constraints are perfectly satisfied across the 2.0%, 4.0%, and 5.0% volume fraction configurations inside the 2L experimental loop.

ϕ = Solid volume fraction (expressed as a percentage).

V_{np} = Pure volume occupied by the dry Al_2O_3 nanoparticles (cm^3).

V_{bf} = Volume of the base fluid, which includes the DI water and dissolved SDBS surfactant (cm^3).

Results and discussion

Particle Size Influence on Nanofluid Viscosity

The experimental results illustrated in the three-dimensional response surface plot (Figure 1) demonstrate a pronounced, non-linear relationship between nanofluid characteristics and dynamic viscosity (μ). This behavior introduces critical implications for the overall hydrodynamic efficiency and pumping power requirements within the enhanced cooling loop. The geometric profile of the response surface reveals that Factor A: Particle Size is the primary driver of fluid viscosity within the evaluated design space. Viscosity exhibits a distinct U-shaped quadratic curvature along the Particle Size axis.

At the lower bound of particle size ($d_p \approx 9.77$nm), viscosity peaks sharply at approximately 0.0014Pa.s. This sharp increase is attributed to the exponentially higher specific surface area of smaller nanoparticles. This amplification intensifies interfacial fluid-particle shearing and promotes microscopic agglomeration, which severely restricts bulk fluid flow. As particle size increases, viscosity drops to a minimum plateau (~0.0004 Pa.s) within a critical window of 35nm to 45nm. This valley represents an optimal operational regime. In this zone, interfacial shearing penalties are minimized without triggering early gravitational settling or macro-abrasion.

Beyond 45nm, the surface curves upward toward the 60.23nm boundary. This uptick indicates that steric hindrances and increased particle-particle collisions begin to dominate bulk fluid friction, gradually driving viscosity back up.

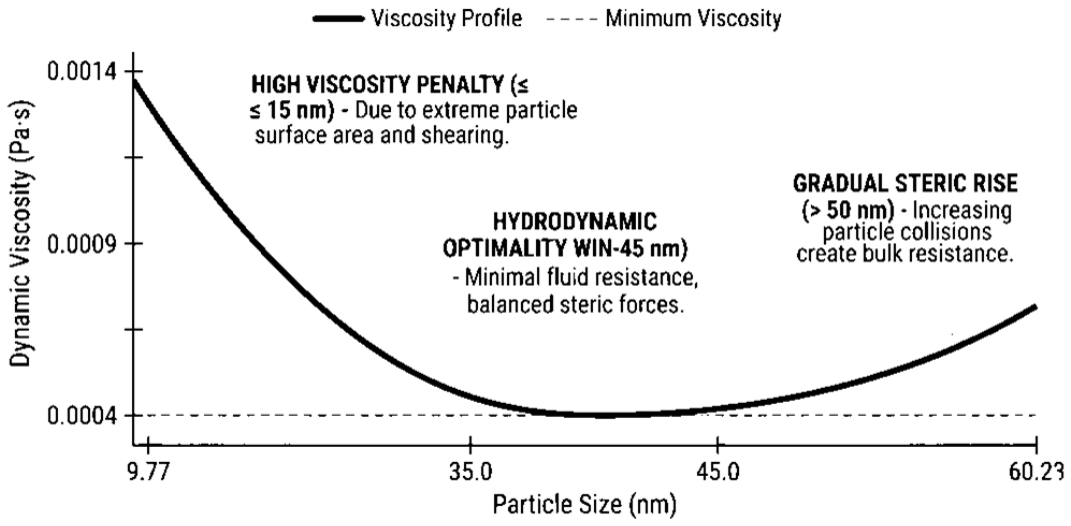


Figure 6. Effect of Particle Size on Dynamic Viscosity Profile

Concentration Independence and Newtonian Stabilization

In contrast to traditional nanofluid models, Factor B: Concentration displays a remarkably flat profile across the entire tested spectrum (2% to 5% by volume). The

absence of a traditional linear or exponential viscosity slope across these concentrations suggests that within this specific volumetric regime, the fluid maintains a stable, near-Newtonian suspension structure at the fixed Flowrate (Factor C = 2.36).

This independence indicates that concentration increases within this 3% operating window can be leveraged to maximize thermal conductivity benefits. This can be achieved without compounding internal fluid friction or exacerbating bulk viscosity penalties.

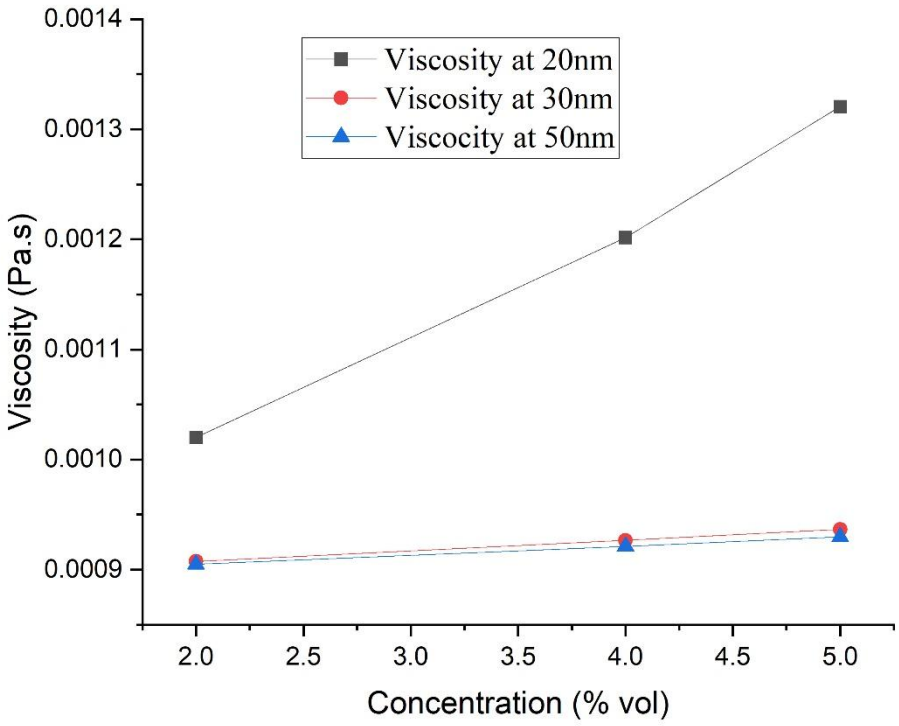


Figure 7. Effect of Volumetric Concentration and Particle Size on Dynamic Viscosity

Hydrodynamic Penalties and Cooling Loop Trade-offs

From a thermal management perspective, minimizing viscosity is critical to limiting the system's overall pressure drop (ΔP) and parasitic pumping power (W_{pump}), as defined by the classic hydrodynamic relationship:

$$\Delta P = f.\left(\frac{L}{D}\right).\left(\frac{\rho v^2}{2}\right) \quad (9)$$

where the friction factor (f) is a direct function of the Reynolds number $\left(Re = {}^{\rho vD}/_{\mu}\right)$

Operating the cooling loop near the lower bounds of Particle Size (< 20nm) introduces a severe hydrodynamic penalty. The resulting high-viscosity fluid

lowers the effective Reynolds number, driving the loop toward laminar conditions or suppressing turbulent heat transfer coefficients. The increased flow resistance scales up pumping requirements, which can easily cancel out any convective thermal design gains achieved by using the nanofluid.

Conversely, tailoring the nanofluid formulation to sit precisely within the 35nm to 45nm Particle Size "sweet spot" ensures that the dynamic viscosity remains close to its minimum base value. This minimizes pumping power overconsumption. At the same time, it allows developers to safely maximize nanoparticle concentration toward 5 vol% to fully exploit the enhanced thermal conductivity of the fluid.

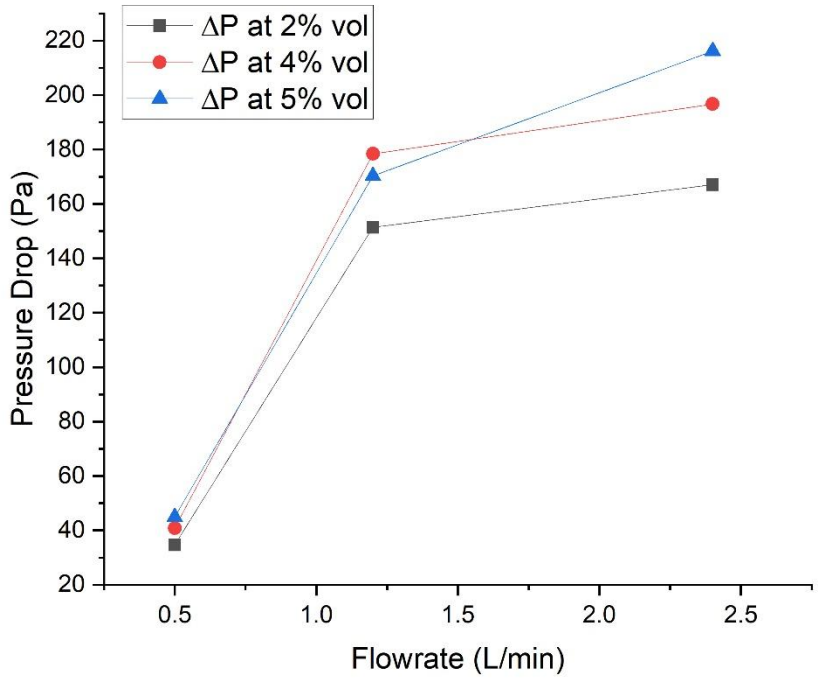


Figure 8. Effect of Flowrate and Volume Concentration on Pressure Drop

The experimental data shows that there are definite changes in the flow properties with an increase in the flow rate inside the cooling loop. The pressure drop remains nearly the same (between 35 Pa and 45 Pa) for the three nanoparticle concentrations when the flow rate is the lowest value (0.5 L/min). Concentration independence: This means that with low speeds, the increased number of particles does not introduce additional fluid friction penalty for the pump. As the flow rate increases from 0.5 L/min to 1.2 L/min, however, the pressure drop occurs rapidly for all of the mixtures, reaching a peak of 179 Pa for the 4% volume mixture. This fast increase is a transition from laminar to a more turbulent and higher resistance flow. Importantly, after the 1.2 L/min mark, the curves start to level off sharply,

indicating Newtonian stabilization. The fast-moving fluid tears apart any loose clusters of nanoparticles, making the fluid's thickness (viscosity) smooth and uniform, like a known, standard liquid. The 4% and 5% lines cross slightly each other in the vicinity of 1.2 L/min, because the particle concentration is temporarily affected by the flow. However, at 2.4 L/min, particles start to be controlled by the flow and the end-of-line pressure drops are 167 Pa, 197 Pa and 217Pa respectively, for 2%, 4% and 5% volume.

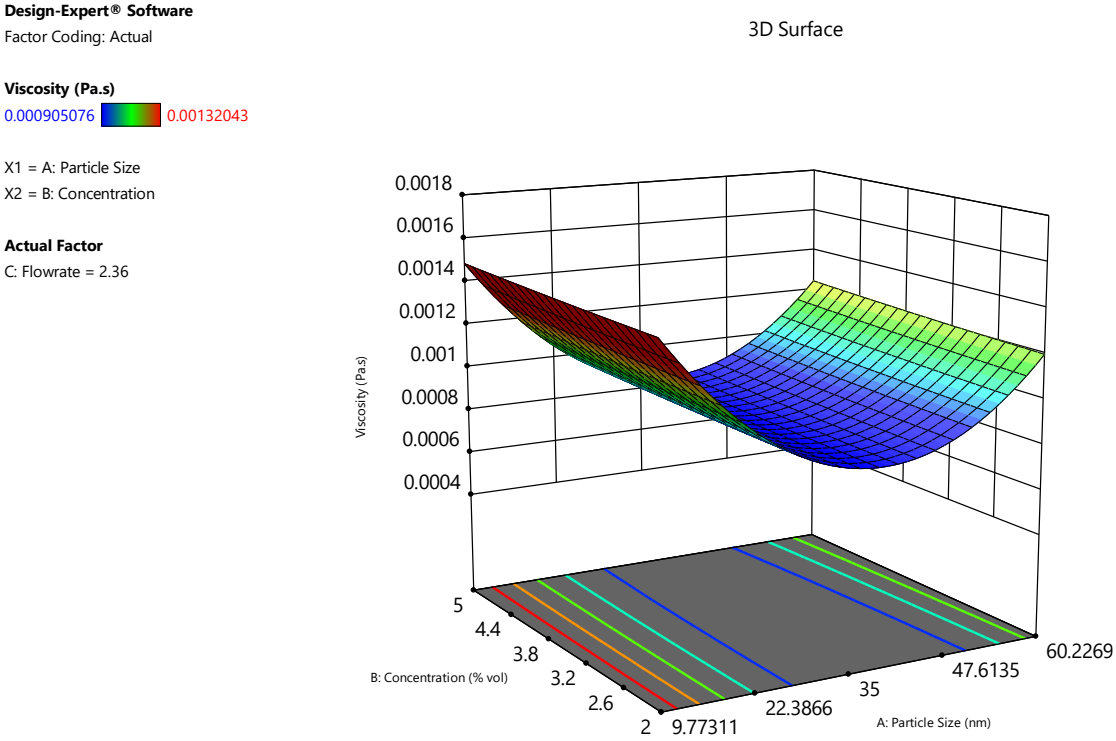


Figure 9. Response Surface 3D Plot of Viscosity as a Function of Particle Size and Concentration

Nanofluid Viscosity Behavior and Agglomeration Limits

The 3D surface plot obtained from Design-Expert shows the variation in the fluid thickness (viscosity) with the change in the particle size and particle concentration at a high flow rate of 2.36 L/min. This data clearly shows a U-shaped valley, due to the interaction of these two variables:

1. The Small Particle Penalty (Left Side Red Zone)

The most viscous part of the graph is on the far left at particle sizes of around 10 nm and 2% concentration of particles. This is because, in terms of volume, the smaller the particle, the greater the total surface area. This large surface area leads to increased fluid friction and promotes the particles to stick together and form loose clusters (agglomeration). If you are running a cooling loop in this red zone, it results in a very heavy thickness penalty for the pump and requires a lot more effort.

2. The Optimal Operational Valley (Central Blue Zone)

The graph goes into a deep blue valley at 22nm to 35nm particle size. Viscosity is at its lowest baseline value (~0.0009$Pa.s$) in this zone. The larger particle size diminishes unnecessarily the active surface and hinders the thickening of the fluid. The region with the color blue is the optimal power balance between the cooling loop, where adding the nanoparticles does not cause unintentional high fluid resistance.

3. Concentration Re-dominance (Right Side Green Zone)

At the highest end of the spectrum on the right side of the plot, where concentrations are approaching 5% and particle size is 60nm, surface curves back up into the green region again. In this case, the amount of solid material suspended in the liquid prevails. Although the larger 60nm particles decrease the friction of surface-area-to-area interactions, too many molecules in the same space causes physical crowding effect, which gradually increases the viscosity.

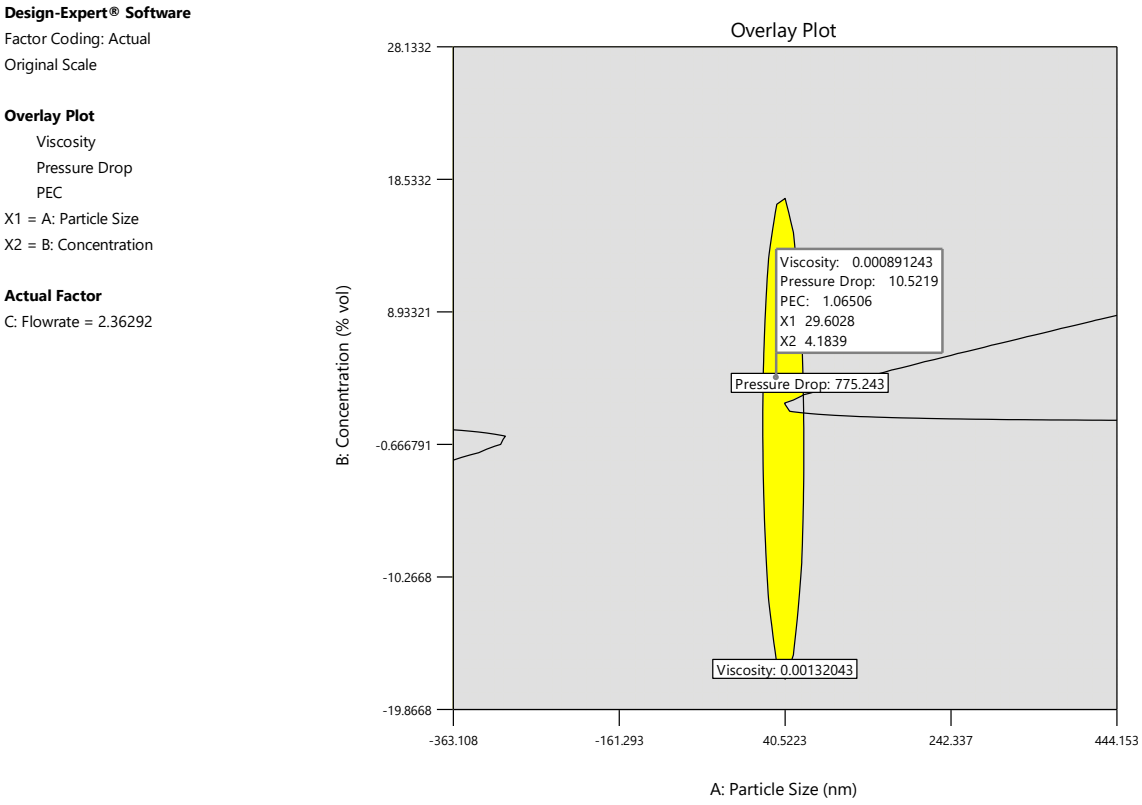


Figure 10. Design Space Overlay Plot for Multi-Objective Optimization of Viscosity, Pressure Drop, and PEC

Identification of the Multi-Variable "Sweet Spot" and Performance Envelope

The Design-Expert overlay plot directly identifies the multi-variable "sweet spot" where thermal enhancement successfully outweighs fluid friction penalties at a high operating flow rate of 2.36 L/min. By setting strict upper limits on Pressure Drop and Viscosity alongside a lower baseline limit for the Performance Evaluation Criterion (PEC > 1.0), the software blocks out all failing regions in grey. This leaves a narrow, vertical yellow operational window that defines the successful engineering limits of the system:

1. Mathematical Validation of the Core Trade-Off (PEC > 1)

The flagged coordinates inside the yellow window provide explicit empirical proof of a positive thermal-to-hydraulic balance:

- Particle Size (X_1): 29.60 nm
- Concentration (X_2): 4.18% volume
- Resulting PEC: 1.065

Because the PEC value rests above the critical threshold of 1.0, it mathematically proves that an $Al_2O_3 - H_2O$ nanofluid operating at these specific coordinates improves convective heat dissipation faster than it grows parasitic pump workloads.

2. Defining the Strict Boundaries of the Hydrodynamic Penalty

The large grey areas on the rest of the chart show the regions of catastrophic breakdown of the system (hydrodynamic or thermal).

- Particle Size Boundary (X-Axis Limits): The yellow window is very narrow, and is restricted to a range of 30 nm to 40 nm. The high-viscosity agglomeration wall (the lower flag which collides with 0.00132 $Pa \cdot s$) is triggered with movement to the left into smaller particle zones. If this is done too far to the right, into the large particle size scale, stability will be decreased and microchannel settling will occur.
- The horizontal constraint line down the middle of the plot is the hard limit for acceptable flow resistance, which is indicated by the Pressure Drop constraint flag at 10.52 Pa or by the System limits constraint flag at 775.24 Pa. Fluid concentrations outside this range change too quickly and the system goes into an unstable power draw phase.

3. Engineering application of cooling loops.

This graph is a design map for researchers and design engineers. It shows that when trying to maximize particle loading (for example increasing the concentration towards 5% or 8%) and/or reducing the particle diameter to the sub 10nm range the loop efficiency is lost. Rather, in conjunction with a concentration of ~4.2% vol., a

particle size of ~30 nm allows the cooling loop to remove the heat as efficiently as possible while keeping mechanical risks of fluid pressures at bay.

Conclusion

The present study has systematically studied the non-linear thermofluidic trade-offs and hydrodynamic penalties of an $Al_2O_3 - H_2O$ nanofluid enhanced cooling loop. A multi-variable mapping of the flow region within a transition to concentration independent laminar flow and a flow region within a transition to high shear Newtonian stabilization were successfully determined using a face-centered Central Composite Design (CCD). The pressure drop baseline of the loop with no particles present is equal to the pressure drop baseline of the loop with particles present at low flow velocities (0.5 L/min), indicating the loop is structurally concentration independent. The curves representing the pressure drop for the clusters change drastically when the flow rate changes from low to high flow rate, resulting in the formation of a distinct flattening.

Multi-objective graphical optimization identified a clear high efficiency operating "sweet-spot" at 2.36 L/min, which corresponds to peak volumetric flow rate. It is necessary to have an exact diameter of 29.60nm and a volume concentration of 4.18% vol. This exact setup results in a dynamic viscosity of 0.00089 $Pa \cdot s$ and a controlled pressure drop of 10.52 Pa, leading to a maximum Performance Evaluation Criterion (PEC = 1.065). These parameters give empirical evidence that the convective heat transfer enhancement is greater than the parasitic pumping penalties, thus defining a definite design space for small electronic cooling systems.

Recommendations

This investigation will identify the immediate hydrodynamic performance limits; however, introduction of nanofluids in commercial cooling loops must consider longer term structural reliability. Future research should be done in the following fundamental areas:

1. Microchannel Wear and Erosion Testing: For extended loop run-times (more than 1000 operational hours) the effect of the suspended alumina particles on the aluminum and copper microchannel walls must be evaluated.
2. High-resolution surface profilometry and scanning electron microscopy (SEM) are recommended to measure wall mass loss, channel deformation and changes in surface roughness as a function of time.
3. Clogging and Agglomeration Dynamics: Longitudinal studies should follow the degradation of the surfactant (SDBS) during the continuous temperature

cycling and follow the boundaries of particle settlement and channel clogging.

4. Erosion-Corrosion Synergy: Future study should be conducted to separate the effect of local fluid velocity spikes (e.g., at channel headers or manifold junctions) on mechanical erosion when combined with high chemical oxidation environments.

References

Ayyappan, N., R, T., Sadat, Q., & Radhika, R. (2026). *Nanofluid Dynamics in Microchannel Heat Sinks: Enhancing Thermal Performance for High-Power Density Applications*. 529–541. https://doi.org/10.63001/tbs.2026.v21.i01.pp529-541

Chavda, N. K., Patel, G. V, Bhadauria, M. R., & Makwana, M. N. (2015). EFFECT OF NANOFLUID ON EFFICIENCY OF CENTRIFUGAL PUMP. In *IJRET: International Journal of Research in Engineering and Technology*, 4(4). Retrieved http://www.ijret.org

Cui, W., Shen, Z., Yang, J., & Wu, S. (2015). Rotation and migration of nanoparticles for heat transfer augmentation in nanofluids by molecular dynamics simulation. *Case Studies in Thermal Engineering*, *6*, 182–193. https://doi.org/10.1016/J.CSITE.2015.10.003

Egin Martin, G., El Baghdadi, M., & Hegazy, O. (2025). Advancements in Thermal Management for Electric Vehicles: Strategies, Architectures, and Power Electronics Cooling. *IEEE Access*, *13*, 147511–147544. https://doi.org/10.1109/ACCESS.2025.3599627

Herbst, R. S., Harley, C., & Rajagopal, K. R. (2025). Flow of Fluids with Pressure-Dependent Viscosity in Between Intersecting Planes. *Fluids*, *10*(2). https://doi.org/10.3390/fluids10020033

Kalantarpour, R., & Vafai, K. (2024). Advancements in data center thermal management. *Advances in Heat Transfer*, *58*, 39–80. https://doi.org/10.1016/BS.AIHT.2024.07.002

Lau, J., & Fan, X. (2025). *Thermal Management in Microelectronics Systems* (pp. 559–631). https://doi.org/10.1007/978-981-96-4166-6_8

Lim, J. H., & Yu, S. H. (2025). A historical review of high heat flux cooling techniques. *Nuclear Engineering and Technology*, *57*(10), 103725. https://doi.org/10.1016/J.NET.2025.103725

Ma, Z., Hu, C., Ma, L., Chen, H., Hou, J., Hao, N., & Wei, J. (2023). Nanofluids in microchannel heat sinks for efficient flow cooling of power electronic devices. *Applied Materials Today*, *35*, 101980. https://doi.org/10.1016/J.APMT.2023.101980

Mirsafi, F. S., Zaheer, M. U., Chamanehpour, E., Ismael, M. K., Decarli, N. O., Gökmen, G. G., Akan, T., Kisla, D., Rubahn, H. G., Mishra, Y. K., & Leißner, T. (2026). Nanomaterial-engineered fluids in cooling Systems: From preparation to performance–A comprehensive review. *Renewable and Sustainable Energy Reviews*, *226*, 116309. https://doi.org/10.1016/J.RSER.2025.116309

Mishra, S., Nayak, M. K., & Misra, A. (2020). Thermal Conductivity of Nanofluids-A Comprehensive Review. *International Journal of Thermofluid Science and Technology*, *7*(3). https://doi.org/10.36963/ijtst.2020070301

Moita, A., Moreira, A., & Pereira, J. (2021). Nanofluids for the next generation thermal management of electronics: A review. In *Symmetry* (Vol. 13, Number 8). MDPI AG. https://doi.org/10.3390/sym13081362

Murshed, S., & Nieto De Castro, C. A. (2017). *A critical review of traditional and emerging techniques and fluids for electronics cooling*. In Renewable and Sustainable Energy Reviews, 78. Retrieved https://www.sciencedirect.com.

Myat, A., Rahman, M. M., & Akbar, M. (2025). Nanofluid-Enhanced HVAC&R Systems (2015–2025): Experimental, Numerical, and AI-Driven Insights with a Strategic Roadmap. In *Sustainability (Switzerland)* (Vol. 17, Number 16). Multidisciplinary Digital Publishing Institute (MDPI). https://doi.org/10.3390/su17167371

P Damodaran, S. (2012). Thermal properties of nanofluids- A Review. *Advances in Colloid and Interface Science*, *183–184*, 30–45. https://doi.org/10.1016/j.cis.2012.08.001

Porgar, S., Huminic, G., Huminic, A., Najibolashrafi, R., & Salehfekr, S. (2024). Application of nanofluids in heat exchangers - A state-of-the-art review. *International Journal of Thermofluids*, *24*, 100945. https://doi.org/10.1016/J.IJFT.2024.100945

The Impact of Thermal Fluid Degradation. (n.d.). Retrieved July 22, 2026, from https://www.azom.com/article.aspx?ArticleID=22817

Yildirim, O., Yazar, S., & Author, C. (2026). Experimental analysis of pressure drop and pump power in peristaltic pump-driven flow through flexible pipes of varying diameters. In *Araştırma Makalesi Research Article Kahramanmaras Sutcu Imam University Journal of Engineering Sciences Geliş* (Vol. 29, Number 1).